Journal of Molecular Structure 1337 (2025) 142083

Contents lists available at ScienceDirect

Journal of Molecular Structure

journal homepage: www.elsevier.com/locate/molstr

Unlocking antidiabetic potential: Novel compounds from endophytic fungi isolated from *Manihot esculenta* Crantz tuberous roots

Keerthana Nagarajan [a], Mahisha Devi Chelladurai [a], Sivaranjini Mani [a], Parasuraman Pavadai [b], Panneerselvam Theivendren [c,*], Ponnusamy Palanisamy [d], Murugesan Sankaranarayanan [e], Selvaraj Kunjiappan [a,*]

[a] Department of Biotechnology, Kalasalingam Academy of Research and Education, Krishnankoil 626126, Tamil Nadu, India
[b] Department of Pharmaceutical Chemistry, Faculty of Pharmacy, M S Ramaiah University of Applied Sciences, Bengaluru, Karnataka 560054, India
[c] Department of Pharmaceutical Chemistry & Analysis, School of Pharmaceutical Sciences, Vels Institute of Science, Technology & Advanced Studies, Pallavaram, Chennai, Tamilnadu 600117, India
[d] School of Mechanical Engineering, Vellore Institute of Technology, Vellore, Tamil Nadu 632014, India
[e] Medicinal Chemistry Research Laboratory, Department of Pharmacy, Birla Institute of Technology & Science Pilani, Pilani Campus, Pilani 333031, India

ARTICLE INFO

Keywords:
Endophytic fungi
Cassava tuberous root
Penicillium oxalicum
Antioxidant
Antidiabetic molecule

ABSTRACT

Penicillium oxalicum is an endophytic fungus isolated from cassava tuberous root (*Manihot esculenta* Crantz), and their ethyl acetate extract tested for free radicals scavenging and α-amylase, β-glucosidase enzyme inhibitory assay. The profiling of molecules from endophytic fungal extract revealed thirteen volatile and four non-volatile bioactive molecules through GC–MS and LC-MS, respectively. Notably, four molecules 2-Phenylpyrido[3,4-d]-1,3-oxazin-4-one (CID: 555,390) -9.40 kcal × mol^{-1}, Guanosine (CID: 135,398,635) -7.60 kcal × mol^{-1}, Quercetin-3-O-sophoroside (CID: 5282,166) -7.60 kcal × mol^{-1}, and Esculin (CID: 5281,417) -7.20 kcal × mol^{-1} were identified for a better binding affinity against PPARγ protein. Molecular dynamics simulation studies predicted the Guanosine-PPARγ complex, which showed highly stable and better intermolecular interactions during the molecular dynamics simulation periods (500 ns). Further, the endophytic fungal extract showed excellent DPPH* and ABTS* scavenging and ferric ion-reducing potentials. Additionally, endophytic fungal extract displayed potential α-amylase and β-glucosidase enzyme inhibitory activities compared to pioglitazone. These findings showed that the ethyl acetate fraction of *P. oxalicum* is an effective source of new antioxidants and possible diabetic inhibitory properties, which can be used to generate prospective antidiabetic drugs.

1. Introduction

Diabetes mellitus is a metabolic condition of the endocrine system that affects carbohydrate, protein, and lipid metabolism due to high blood sugar levels in the blood [1]. It is a multifaceted disease that disease that rates among the top causes of death, especially when deadly complications are considered [2]. The number of patients with diabetes has profoundly increased worldwide. Type 2 diabetes mellitus (T2DM) has afflicted approximately 400 million people, and it is projected to go over 600 million people by 2035 [3]. Consumption of carbohydrates-rich or high protein or fats-rich foods, highly processed food, junk food, alcohol with smoking, less physical activities, etc., are the main reasons for the postprandial hyperglycemia with the development of the complete symptomatic representation of T2DM [4]. Diabetes happens due to inadequate insulin secretion from the pancreas, impaired insulin sensitivity, or insulin resistance; muscle cells, fat, and the liver don't respond to insulin and can't take up glucose from the blood [5]. As a result, the pancreas secretes more insulin to help glucose enter the cells. Hyperglycaemia, insulin resistance, and oxidative stress are the leading causes of T2DM [6]. As a result of excessive glucose and oxidative phosphorylation, mitochondria produce more reactive oxygen species (ROS) and experience more oxidative stress [7]. Furthermore, prolonged hyperglycaemia and elevated ROS levels contribute to the development of atherosclerosis (cardiovascular complication) [8]. Diabetic people also suffer retinal, renal, and nerve damage, which leads to early death [9]. ROS can be produced by nonenzymatic glycosylation, the electron transport chain in mitochondria, and membrane-bound NADPH oxidase [10].

* Corresponding authors.
E-mail addresses: tpsphc@gmail.com (P. Theivendren), selvaraj.k@klu.ac.in (S. Kunjiappan).

https://doi.org/10.1016/j.molstruc.2025.142083
Received 6 November 2024; Received in revised form 9 March 2025; Accepted 14 March 2025
Available online 19 March 2025

The nuclear hormone receptor superfamily's peroxisome proliferator-activated receptors (PPARs) proteins are fatty acid-activated transcription factors that control energy metabolism [11]. The transcription factor PPARs are three subtypes, such as PPARα, PPARγ, and PPARδ (sometimes called PPARβ) [11]. They are critical players in regulating lipid and carbohydrate metabolism [12]. Also, PPARs have a significant regulatory role in maintaining energy homeostasis; each PPAR possesses unique activities and specific expression locations. PPARγ is a prominent regulator of adipose cell differentiation and formation [13]. The class of antidiabetic drugs known as TZD (Thiazolidinediones), which encompasses Rosiglitazone (Rosi, Avandia) and Pioglitazone (Pio, Actos), is generally recognized for its specific target protein. The inhibition of PPARγ has been observed to selectively augment or partially replicate the distinct effects of insulin in individuals diagnosed with type 2 diabetes mellitus (T2DM) [14].

Moreover, the inhibition of PPARγ exhibits an additive effect when combined with other antidiabetic agents such as sulphonylureas (glipizide (Glucotrol), Gliclazide, glimepiride (Amaryl), and Tolbutamide), metformin (Glucophage), and acarbose, resulting in a reduction in the necessary insulin dosage for patients on insulin treatment [15]. The TZD function as complete agonists of PPARγ and have significant efficacy as oral pharmaceuticals in managing T2DM from a clinical standpoint [16]. However, numerous clinical investigations have demonstrated that the use of these TZD is linked to various adverse effects, including obesity, fluid retention, weight gain, heart hypertrophy, hepatotoxicity, and loss of bone mineral density [17–19]. For example, Avandia's (Rosiglitazone) withdrawal from the European market and subsequent restrictions imposed by the FDA can be attributed to the heightened cardiovascular risks linked to its utilization [20]. In recent times, Actos (Pioglitazone) has been associated with a multitude of contentious adverse effects, notably the heightened susceptibility to bladder cancer [21]. Given the escalating worldwide prevalence of T2DM, it is evident that there exists a pressing imperative to explore and create innovative anti-diabetic medicines that specifically target PPARγ, hence enhancing their therapeutic efficacy with less/nil adverse effects. Therefore, an endophytic fungus isolated from cassava root has identified a novel anti-diabetic molecule.

Many ethnic groups have used cassava (*Manihot esculenta* Crantz) as a traditional medicine because of its many pharmacological uses, which include its ability to prevent diabetes [22]. Cassava tuber has excellent nutritional value and is known to contain alkaloids and other flavonoid glycosides [23]. Flavonoids have antioxidant and hypolipidemic properties, while glycosides are effective against heart disease [24]. The endophytic fungus residing within the plant tissue may directly or indirectly contribute to the plant's growth, stress tolerance, phytohormone regulation, and disease resistance [25]. Endophytic fungi are a possible source of peptides, enzymes, secondary metabolites, and other compounds that promote health and are utilized in medicines and healthcare sectors [26]. Secondary metabolites of endophytic fungi are a potential source of antioxidant and antidiabetic drugs [27]. The present work aims to screen and identify antioxidant, α-amylase, and β-glucosidase enzyme inhibitors from an endophytic fungus isolated from cassava root. Further, identification of anti-diabetic molecules from screened molecules of endophytic fungal extract against PPARγ receptor through molecular docking approaches. Molecular dynamics simulation studies determine stability and intermolecular interactions between predicted molecules with the target protein PPARγ receptor.

2. Materials and methods

2.1. Materials

Himedia Laboratories, Pvt., Ltd., Mumbai, India, supplied the following chemical and reagents, 2,2-diphenyl-1-picrylhydrazyl (DPPH), 2,2′-Azinobis (3-ethylbenzothiazoline-6-sulphonic acid) (ABTS), 2,4,6-Tris(2-pyridyl)-s-triazine (TPTZ), lactophenol, aluminium chloride, sodium carbonate, sodium nitrite, aluminum chloride, rutin, Potato dextrose agar (PDA) medium, porcine pancreatic α-amylase, β-glucosidase. All other reagents, solvents and various chemicals (analytical grade) are supplied by Merck and SD Fine Chemicals in Mumbai, India.

2.2. Plant sample collection and screening of endophytic fungi

The cassava tuberous roots were harvested from farmland in Kunnar village (Latitude: 9.5121425° N and Longitude: 77.6340799° E), Srivilliputhur (Taluk), Virudhunagar District, Tamil Nadu, India, in November 2023. A botanist at Ayya Nadar Janaki Ammal College in Sivakasi, Tamilnadu, validated the plant. The endophytic organisms were isolated according to our previous approach [28]. In brief, the harvested tuberous roots were washed with running tap water 1–3 times and subsequently rinsed with de-ionized water to eliminate soil debris and unwanted waste. The tuberous roots were thoroughly cleaned and chopped into little pieces (1 cm × 0.5 cm) under sterile conditions. The tuberous root surface was sterilized by dipping it in 70 % ethanol for 60 s, followed by a 6-minute immersion in 1 % sodium hypochlorite. The tuberous root was rinsed again using sterile deionized water. The sterile root sample was pulverized using a sterile mortar and pestle before being diluted in sterile water stepwise. Then, 50 μL of ten-fold diluted cell suspension was plated in potato dextrose agar (PDA) plates with a pH of 5.6 ± 0.02 and kept at 27 °C for 4–7 days. Control plates were also maintained to detect contamination. Every 24 h, the endophyte growth on the plates was monitored. After the specified time interval, the plates were examined for the growth of fungal mycelial colonies containing spores. Afterward, unique single fungal colonies were subculture on PDA plates. The morphology and color of several colonies were observed without opening the plate. The morphological observations of the mycelial colonies were examined under a microscope using a lactophenol cotton blue mount. Mycelia and conidiophores were seen on the slides using an optical microscope at 40 × magnification. The growth rates of the endophytic fungi were studied by measuring the colonization frequency (CF %) in the below Eq. (1):

$$\%CF = (A / B) \times 100$$

Where A=Number of segments colonized by fungi; B = Total number of segments observed

2.3. Molecular identification of endophytic fungi

The molecular gene sequencing technique was performed to identify the endophytic fungal species residing in the plant [29]. Lysis solution (50 mM Tris Hydrochloride (pH 8.0), 0.7 M NaCl, 20 mM EDTA, 2 % CTAB (cetyltrimethylammonium bromide), 1 % β-mercaptoethanol, and 1 % polyvinylpyrrolidone 40) used to extract fungal DNA. Briefly, 100 mg of fungal mycelia and 500 μL of lysis solution were vortexed for 30 min at 65 °C in a water bath before being centrifuged for 10 min at 10, 000 rpm. The collected supernatant was mixed with 600 μL of binding buffer and stored for 5 min at 25 °C. Further, the mixture was carefully transferred to a spin column and centrifuged at 12,000 rpm for 2 min. A residual mixture can be re-assembled when added to the spin column. The spin column was cleaned with 500 μL of washing buffer I and centrifuged for 2 min at 12,000 rpm, and the flow-through was removed. Similar washing procedures were performed with 500 μL of washing buffer II, and the spin column was carefully transferred to a fresh microcentrifuge tube, after which the fungal DNA was eluted with 100 μL of elution buffer and subjected to centrifugation at 12,000 rpm for 2 min. An aliquot of eluted fungal DN A was electrophoresed on a 0.8 % agarose-EtBr gel, and the concentration was calculated with Qubit 3.0. The isolated fungal DNA was used as a template for polymerase chain reaction (PCR) amplification of the internal transcribed spacer (ITS) region containing 5.8 s rDNA, with typical ITS 1 and ITS 4 primers.

Previous reports guided the selection of reaction components for ITS region amplification. The thermal cycler was initially configured to denaturation at 94 °C for 5 min, followed by 30 cycles of denaturation at 94 °C for 30 s, annealing at 50 °C for 30 s, and initial extension at 72 °C for 1 min. Furthermore, the last extension was carried out at 72 °C for 5 min to avoid unamplified amplicons. The PCR product was electrophoresed in 1.2 % agarose-EtBr, and the amplicons were sequenced with macrogen. The resulting sequences were fed into Nucleotide BLAST and compared to known gene sequences. The ITS sequences obtained in this work and those obtained from the NCBI database were trimmed by removing primer annealing areas and aligned with MEGA X. HKY85 (Hasegawa-Kishino-Yano, 85) was found as the best feasible substitution matrix for the aligned sequences using MEGA X, as it had the lowest Bayesian Information Criterion (BIC) score. Various statistical approaches were used to generate a phylogenetic tree. The Neighbor-Joining statistical technique determined the evolutionary relationship, and distances were calculated using the maximum likelihood method. Finally, the optimum tree was created and tested using 1000 bootstrap.

2.4. Isolation of fungal metabolites

The ultrasound-mediated extraction approach was utilized to separate secondary metabolites of bioactive molecules from the chosen fungus, with ethyl acetate as the extraction solvent [30]. The extraction process involved 500 mg of a pure culture of the isolated fungus and 10 mL of 80 % ethyl acetate. This extraction was carried out in an adjustable ultrasonic bath sonicator with a modifiable temperature of ± 1.0 °C, a power of 220 V, and a continuous mode at 20 kHz high-intensity ultrasound processor. The sonicator had a jacketed reactor with a capacity of 250 mL and was created by PCI Analytics Ltd. in Mumbai, India. The ultrasound intensity used was 80 W cm2, with a pulse cycle of 0.5 and a temperature of 40 °C. After the ultrasound-assisted extraction, the extract was filtered and centrifuged at 2600 g for 5 min using Whatman No 1 filter paper. The volatile and non-volatile nature of the components in the fungal ethyl acetate extract filtrate was determined using GC–MS and LC-MS analyses.

2.5. Identification of bioactive molecules

Gas chromatography-mass spectroscopy (GC–MS) and liquid chromatography-mass spectroscopy (LC-MS) are used to examine endophytic fungal samples in order to identify both volatile and non-volatile molecules [4]. The Shimadzu Make QP-2010 equipment was utilized to execute the GC–MS analysis. In the context of GC-MS detection, a non-polar 60 M RTX 5MS column was used, with helium serving as the carrier gas. The column was maintained at a constant pressure of 15 psi and a determined column flow velocity of 1.00 mL × min^{-1}. The injector was employed at 250 °C, and the oven temperature was programmed as follows: 60 °C for 15 min, then gradually increased to 280 °C at 3 min. The bioactive components were identified by analyzing the retention time of chromatographic peaks using a Quadrapole detector. The relative retention indices were determined using the Wiley and NIST 2014 library (National Institute of Standards and Technology, 2014). Agilent Technologies, USA, utilized the 1290 Infinity UHPLC System and 6550 iFunnel Q-TOFs for the LC-MS study. The Zorbax-SB-C-18 column used for separations has a particle size of 1.8 µM and a 2.1 × 50 mm diameter. In this experiment, two mobile phases were employed: A-0.1 % formic acid in water and B-90 % acetonitrile in water. The flow rate was maintained at 500 µL × min^{-1}. The LC conditions were kept at a 5 % concentration in B for 0–3 min. The concentration gradually increased from 5 % to 20 % between 3 and 25 min, from 20 % to 40 % between 25 and 40 min, and from 40 % to 50 % between 40 and 55 min. Finally, the concentration reached 50 % to 95 % at 55–63 min. Positive and negative peak detection modes were conducted using a direct injection with an Electron Spray Ionization (ESI) probe. Bioactive molecules were determined non-volatile using online libraries to get the molecular mass and structural formula.

2.6. In silico molecular docking

Gas chromatography and liquid chromatography with mass spectrum analyses were conducted to determine the therapeutically valuable molecules in the endophytic fungal extract. The identified molecules were docked against the probable target of PPARγ (peroxisome proliferator-activated receptor gamma in complex with ZINC5672437, PDB: 8FHF) [31]. The crystallographic structure of the protein target was downloaded from the Research Collaboratory for Structural Bioinformatics Protein Data Bank (RCSB PDB). Chemsketch software was used to construct a three-dimensional structure of the molecules found during GC–MS and LC-MS examinations of fungal extract. The structures were subjected to rigorous optimization and reduction methods using Auto Dock Vina technologies and BIOVIA Discovery Studio. The produced structures were transformed into .pdb file format using the BIOVIA|Discovery Studio v20.1.0.19295 software (Accelry's Software Inc., San Diego, USA).

2.7. Molecular dynamics (MD) simulation

Molecular dynamics simulations of protein-ligand complexes were carried out using Desmond dynamic package 2017 in Schrodinger (academic version) on a Linux background to study the changes with the solvent system in complexes. The complex's time-dependent evolution was calculated for 500 nanoseconds. The OPLS forcefield was used for the MD simulation of the docked complex (PPARγ-ligand) [32]. To simulate dynamics, the complex was centered in an orthorhombic cubic box with TIP3P water molecules and buffers at a distance of 10 Å from the box edge and protein atom [33]. The volume of the boundary condition box was calculated based on the complex type. Counter ions, such as Na^+ and Cl^-, were randomly introduced to neutralize the system. The Desmond protocol with OPLS-2005 forcefield settings minimized the solvated constructed system, followed by relaxation. The Berendsen NVT ensemble was employed to model the system, with the temperature maintained at 10 K to restrict the movement of heavy atoms in the solute. The MD simulation was conducted at a temperature of 300 K, pressure of 1 atm, and with a thermostat relaxation time of 200 picoseconds. The simulation was performed under an isothermal isobaric ensemble (NPT). During molecular dynamics (MD) simulations, the Nose-Hoover thermostat and the Martyna-Tobias-Klein barostat methods have kept the temperature at 300 K and the pressure at 1 atm, respectively [34]. The simulation's progress was meticulously documented at regular intervals of 50 picoseconds. The NPT ensemble was launched after a 100 ns simulation. In order to analyze the paths followed by objects, the frames were collected and scrutinized using the simulation interaction diagram, which facilitated the identification of fluctuations.

2.8. Density functionality theory

Gauss View molecular visualization tool used to draw the molecular structure of chosen bioactive molecules. Using the Gaussian 03 W software package, the bioactive compounds' molecular geometry was optimized using density functional theory at the B3LYP level and the 6–31G+ (d,p) basis set. The molecular electrostatic potential, maximum occupied molecular orbital (HOMO), and lowest unoccupied molecular orbital (LUMO) energy were calculated using Gaussian 09 W software using the optimized structure of bioactive molecules. The vibrational frequencies were measured at the same level of theory for the optimized geometry, and the discovered frequencies were scaled to 0.9614 [35].

2.9. Antioxidant assay

2.9.1. DPPH radicals scavenging assay

The DPPH free radicals scavenging efficacy of the endophytic fungal extract was estimated using a DPPH solution (prepared by dissolving 8 mg of DPPH in 100 mL of 95 % ethanol) according to our previous method, with some modifications [36,37]. Concisely, 3 mL of endophytic fungal extract (at concentrations of 10, 25, 50, 100, and 150 μg/mL) and the blank were separately mixed with 1 mL of DPPH reagent. Then, the mixture was kept at 37 °C for 30 min. After 30 min, a UV–visible spectrophotometer was used to measure the absorbance at 517 nm. The rutin was used as a reference for comparison. The % DPPH free radical scavenging capacity was measured as Eq. (1):

$$\%\ \text{DPPH free radical scavenging capacity} = ((A - B)\times 100)/A \quad (1)$$

where A-absorbance of the control and B-absorbance of the sample.

2.9.2. %ABTS radicals scavenging assay

This assay examined the capacity of the fungal extracts to neutralize the ABTS free radical cations. 5 mL of 4.9 mM potassium persulfate and 5 mL of 14 mM ABTS (v/v) reagent were combined to create the ABTS radical cation reagent and left in the dark for 12 to 16 h. The ABTS solution was diluted with 0.3 mL of ethanol after thoroughly mixing it with 100 μL of the fungal extract (10, 25, 50, 100, and 150 $\mu g \times mL^{-1}$). The absorbance of the reaction mixture was computed at 734 nm and adjusted to 0.700 (0.0020) using a UV–visible spectrophotometer with distilled water as a blank. The results were compared to the control, which consisted solely of ABTS solution after the reaction mixture was incubated for 6 min. Eq. (2) shows the standard curve that was used to estimate the%ABTS free radicals scavenging activity. It uses rutin in 80 % ethanol as the reference standard [38,39].

$$\%\ \text{ABTS radical scavenging activity} = ((A_0 - A_1)\times 100)/A_0 \quad (2)$$

where A_0-absorbance of the control and A_1-absorbance of the sample.

2.10. Ferric-reducing antioxidant potential (FRAP) assay

The effectiveness of the endophytic fungal extract in ferric ions reducing potential was assessed using the prescribed procedure [40,41]. The method employed electron-donating molecules to transform Fe^{3+} TPTZ (a colorless complex) into Fe^{2+} TPTZ (a blue complex) under acidic conditions. The change in absorbance at a wavelength of 593 nm was used to observe this phenomenon. The FRAP reagent was made by combining 3.1 *g* of sodium acetate and 16 mL of acetic acid in a 300 mM acetate buffer at a pH of 3.6. A 10-mM TPTZ solution in 40 mM hydrochloric acid and a 20 mM solution of $FeCl_3{\cdot}6H_2O$ were included. Before adding $FeCl_3{\cdot}6H_2O$, mix the acetate buffer (25 mL) and TPTZ (2.5 mL). In order to determine the absorbance at a wavelength of 593 nm, 40 μL of endophytic fungal extract with concentrations of 10, 25, 50, 100, and 150 $\mu g \times mL^{-1}$ were combined with newly prepared FRAP reagent in a dark environment and maintained at a temperature of 37 °C for a duration of 30 min. The linearity of the standard was maintained over $FeSO_4$ concentrations ranging from 200 to 1000 M. The results were reported as the amount of Fe (II) in moles per gram. Rutin was used as the benchmark reference standard to compare the fungal extracts.

2.11. Non-cellular antidiabetic assay

2.11.1. α-amylase inhibitory activity

To prepare a 4 Unit $\times$ mL^{-1} solution, 1 mL of porcine pancreatic α-amylase was dissolved in 9 mL of 20 mM phosphate buffer (pH 6.9). 1 mL (10, 25, 50, 100, and 150 $\mu g \times mL^{-1}$) of endophytic fungal extract was mixed with 5 mL of 2 % DMSO. Potato starch (0.5 % w/v) was dissolved in 20 mM phosphate-buffered saline (pH 6.9) and heated in a boiling water bath to create a transparent solution. The α-amylase inhibitory assay executed utilizing a chromogenic non-pre-incubation method was adopted [42]. In a screw-capped plastic tube, 20 μL of endophytic fungal extracts were mixed with 200 μL of starch solution and 80 μL of distilled water. To initiate the reaction, add 100 μL of enzyme solution to the tubes and kept at 25 °C for 3 min. The enzyme solution was added at 1-minute intervals from the start of the process. To begin, 100 μL of the mixture was withdrawn into a separate test tube containing 50 μL of DNS colour reagent (50.68 g sodium potassium tartrate mixed in 70 mL of 2 M NaOH with 0.026 mM of 3,5-dinitro salicylic acid) and placed in a water bath heated at 90 °C for 15 min. Dilute the mixture in each tube with 4.50 mL of distilled water, then measure absorbance at 540 nm. To compensate for the absorbance generated by the endophytic fungal extract, blank incubation was conducted by replacing the enzyme solution with 100 μL of distilled water at the start of the reaction. Control incubations were executed with 40 μL of 2 % DMSO instead of the endophytic fungal extract to ensure complete enzyme activity. All experiments were performed in duplicate. The maltose percentage (w/v) was evaluated using the maltose standard calibration curve equation (0–0.1 % w/v maltose). To determine α-amylase inhibition, use the below Eq. (3):

$$\alpha - \text{amylase inhibition}\ (\%) = 100 - \%\text{reaction}\ (\text{at t} = \text{min}) \quad (3)$$

where,% reaction = (mean maltose in sample × 100) / mean maltose in control.

2.11.2. β-glucosidase inhibitory activity

The inhibitory activity of the endophytic fungal extract against β-glucosidase was assessed using a 96-well plate, as described in a prior study [43]. In brief, a total of 20 μL of substrate (p-nitrophenyl-β-d-glucopyranoside, with a concentration of 1 $mg \times mL^{-1}$), 10 μL of endophytic fungal extract (at concentrations of 10, 25, 50, 100, and 150 $\mu g \times mL^{-1}$), and 20 μL of pH 5 sodium phosphate buffer solution were combined on a 96-well plate. The mixture was then incubated at 37 °C for a duration of 10 min. Next, 10 μL of a solution containing β-glucosidase enzyme at a 5 mg × mL−1 concentration was introduced. The resulting combination was then incubated for an additional 30 min at a temperature of 37 °C. A volume of 140 microliters of buffer solution with a pH of 10 and a concentration of 50 mM was introduced to halt the process. The positive control consisted of a mixture of solvents instead of the extract, while the negative control involved using pH 10 buffer at the beginning of the test to prevent enzyme activity. The absorbance was quantified at a wavelength of 410 nm, and the degree of inhibition was calculated using Eq. (4) provided below:

$$\%\ \beta - \text{glucosidase inhibition} = 100 - [(A - B/C) \times 100] \quad (4)$$

Where, *A*= absorbance of test sample; *B*= absorbance of negative control; *C*= Absorbance of positive control

2.12. Statistical analysis

SPSS statistical software (SPSS Inc., Chicago, IL, USA, version 20.0 software) was used to assess the experimental data. All experiments and their outputs were performed three times, and the numerical results are stated as mean ± standard deviation (SD). A value of $p < 0.05$ was significant.

3. Results

3.1. Fungal isolation and morphological confirmation

Five attempts were executed to screen and identify the endophytic fungal species from the cassava tuberous root. Seven endophytic fungal colonies were found in the potato dextrose agar medium. Each fungal colony was isolated and purified by moving successive hyphal tips throughout two to three passes. Better fungal species were preferred for

phylogenetic study on the basis of fungal colonization frequencies (CF %) and the antioxidant efficacy of the fungal extracts. The selected fungi had a growth rate of 79 ± 3.2 % and a biomass yield of 2.8 ± 0.75 $g \times L^{-1}$. It has mycelia dissolved in the medium and is silky and white in appearance. Fig. 1 shows the individual isolated fungus from the mixture culture.

3.2. Phylogenetic analysis

Character-based and distance-based strategies were used in constructing the phylogenetic tree. Using multiple approaches for phylogenetic analysis, the same topology was discovered. Using the fungal DNA sequence, the Neighbor-Joining method was employed to estimate the phylogenetic evolutionary links. The optimal phylogenetic tree illustrates how the various species of the genus Penicillium are arranged as separate branches based on their morphological population. These results are validated by the maximum likelihood technique, which was used to compute the evolutionary distances of the best tree. The ITS sequence data from this investigation demonstrated a similarity of about 92 % and is categorized with *Penicillium oxalicum* sequences (accession number of eukaryotic nuclear mRNA/*Manihot esculenta* fungi: PV123085) (Fig. 2). It has been demonstrated that the unidentified isolate B1 employed in this work may be *Penicillium oxalicum*, the most likely species, based on similarities (92 %), ITS sequence data, and the result drawn from phylogenetic analysis.

3.3. GC-MS and LC-MS molecule prediction

Seventeen peaks were observed from the GC–MS chromatogram of the ethyl acetate extract of endophytic fungi *Penicillium oxalicum.* The identification of the bioactive molecules was accomplished by comparing their peak retention time, peak area (%), height (%), and mass spectral fragmentation patterns to those of the known molecules deposited in the National Institute of Standards and Technology (NIST) collection. Among the seventeen peaks, thirteen bioactive molecules (based on molecular structure) were identified from the GC-MS spectrum (Fig. 3). Table 1 presents the identified bioactive molecules and their molecular structures, formula, and mass. Further, LC-MS is an essential tool to identify potential non-volatile molecules present in the *Penicillium oxalicum* ethyl acetate extract. The LC-MS chromatograms exhibited several peaks in both positive and negative modes (Fig. 4). A total of four molecules were identified in both modes. In the positive mode two molecules were identified, namely, Guanosine (retention time: 13.399 min; formula: $C_{10}H_{13}N_5O_5$; mass: 283.24 g × mol^{-1}), and quercetin-3-O-sophoroside (retention time: 18.164; formula: $C_{27}H_{30}O_{17}$; mass: 627.37 g × mol^{-1} and in the negative mode, Linamarin (retention time: 22.776; formula: $C_{10}H_{17}NO_6$; mass: 247.24 g × mol^{-1}), and Esculin (retention time: 14.678; formula: $C_{15}H_{16}O_9$; mass: 340.28 g × mol^{-1}).

Fig. 1. The individual separated the endophytic fungus (*Penicillium oxalicum*) from the mixture culture.

3.4. Molecular docking

Structure-based molecular screening tests were conducted to predict potent binding compounds against the target protein (PPARγ, PDB id: 4XUM) derived from the PDB database. The chosen top-scored molecule interactions with the PPARγ protein were interpreted utilizing the BIOVIA Discovery studio visualization tool. The active molecules interact with the target PPARγ protein 2-Phenylpyrido[3,4-d]−1,3-oxazin-4-one (CID: 555,390) with a binding score of −9.40 kcal × mol^{-1}, Guanosine (CID: 135,398,635) with a binding score of −7.60 kcal × mol^{-1}, Quercetin-3-O-sophoroside (CID: 5282,166) with a binding score of −7.60 kcal × mol^{-1}, and Esculin (CID: 5281,417) with a binding score of −7.20 kcal × mol^{-1} (presented in Table 2). The image shows interactions within the 4XUM_555,390 complex, focusing on a ligand and its binding with surrounding residues. The 2D interaction diagram highlights key amino acids such as Ser289, Phe281, and Leu469, with red spikes indicating hydrophobic contacts and dotted lines showing hydrogen bonds. The 3D view of the binding pocket, with green dashed lines representing hydrogen bonds and other interactions. These results suggest that hydrogen bonding and hydrophobic interactions play a significant role in the ligand's binding stability, potentially contributing to its inhibitory effect on the target Figs. 5(a) and (b). The 4XUM_135,398,635 complex depicts ligand interactions within the binding pocket of the target protein. A 2D interaction map highlights critical residues, including Cys285, Phe282, and Tyr473, with red spikes representing hydrophobic interactions and dotted lines for hydrogen bonds. The distances suggest strong binding contacts, enhancing ligand stability. In a 3D visualization of the pocket, with green dashed lines showing hydrogen bonds. This analysis indicates a well-defined binding pocket where both hydrophobic and hydrogen-bonding interactions contribute significantly to the ligand's binding affinity and potential inhibitory effect Figs. 5(c) and (d). The image shows the 4XUM_5,282,166 complex, illustrating ligand interactions within the target protein's active site. In a 2D interaction diagram highlights significant residues, such as Glu343, Ser342, and Arg280, with hydrophobic interactions represented by red spikes and hydrogen bonds indicated by dotted lines. Like those to Glu291 and Glu343, key binding distances suggest strong anchoring points. Green dashed lines denote hydrogen bonds in a 3D view of the binding pocket. This structural visualization underscores the importance of both hydrophobic and hydrogen-bonding interactions for ligand affinity and stability Figs. 5(e) and (f). The image represents the 4XUM_5,281,417 complex, highlighting ligand interactions within the protein binding pocket. 2D interaction diagram shows a where residues like Phe363, His449, and Ser289 form key interactions with the ligand. Red spikes indicate hydrophobic interactions, while hydrogen bonds are marked with green dotted lines, with notable bonds between Ser289 and His449. The 3D view provides with green dashed lines illustrating hydrogen bonds and other stabilizing contacts. The combined visualization suggests strong binding facilitated by hydrophobic interactions and hydrogen bonding, which may enhance the ligand's inhibitory potential and stability in the pocket Figs. 5(g) and (h).

3.5. Molecular dynamics simulation

The 4XUM_555,390 complex was analyzed via molecular dynamics simulation to assess the stability and interaction profile of the ligand within the protein's binding pocket. Root Mean Square Deviation

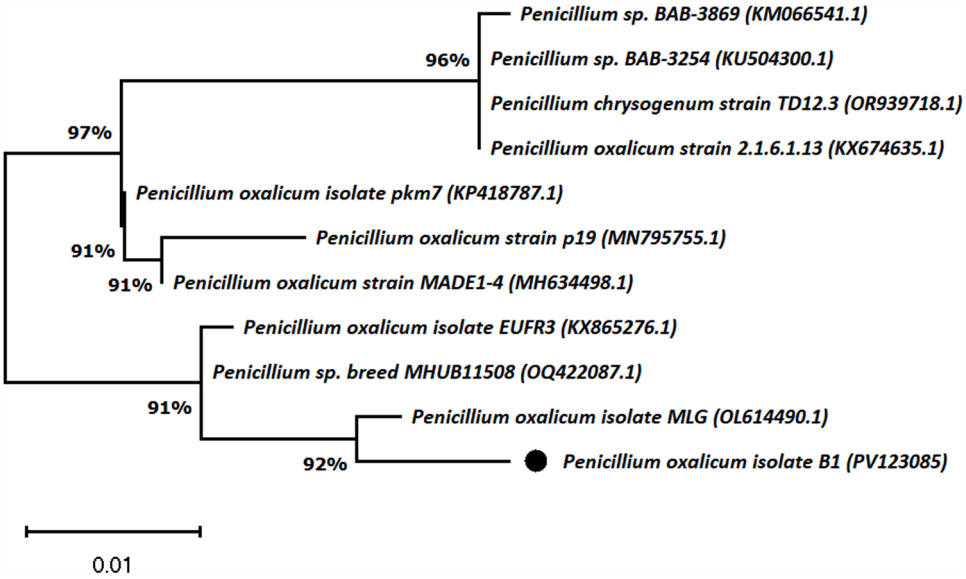

Fig. 2. Phylogenetic tree showing the relationship among endophytic fungi and other fungal species isolated from *Manihot esculenta* Crantz Tuberous Roots. ITS sequences of the genus Penicillium sequences were used to infer the phylogenetic relationship of the unidentified isolate B1. Phylogenetic relationships derived from Maximum likelihood analyses of concatenated ITS datasets.

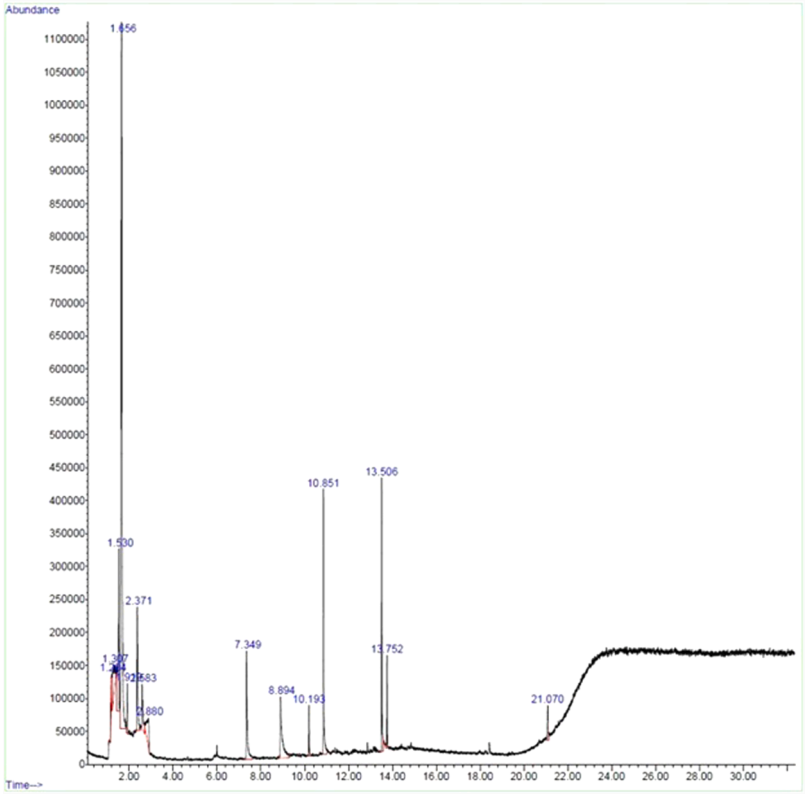

Fig. 3. GC–MS spectrum of ethyl acetate fraction of endophytic fungal extract.

(RMSD) values for both protein and ligand indicate a stable complex formation, as both maintain consistent deviation values after an initial equilibration phase. This stability is further supported by Root Mean Square Fluctuation (RMSF) data, which show minimal fluctuation in core protein residues, suggesting rigid binding site regions with minimal conformational change over time. Hydrogen bonding and hydrophobic contacts are significant, with residues such as Ser289 and His449 forming stable hydrogen bonds with the ligand. Hydrophobic interactions with residues like Phe363 and Leu469 contribute to the ligand's affinity and positioning within the pocket, reinforcing the ligand's binding stability. The ligand's radius of gyration (rGyr) and solvent-accessible surface area (SASA) data confirm its compact, stable conformation, which minimizes exposure to solvent molecules and potentially enhances its bioavailability. This analysis demonstrates that the ligand binds effectively within the protein pocket, supported by a stable network of interactions. These findings suggest that the ligand

Table 1
Identified molecules from ethyl acetate fraction of endophytic fungal extract.

Retention Time	% area of peak	Molecule	Molecular Formula	Molecular weight (g × mol^{-1})	structure
GC–MS analysis					
1.204	2.57	1H-Imidazole	C3H4N2	68.08	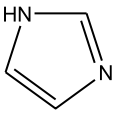
1.307	3.52	2-Phenylpyrido[3,4-d]−1,3-oxazin-4-one	$C_{13}H_8N_2O_2$	224.21	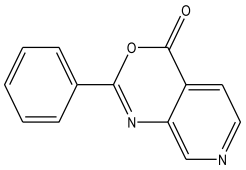
1.530	6.33	Pentanamide	C5H11NO	101.15	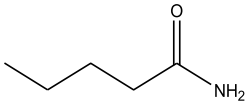
1.530	6.33	dl-Erythro-O-methyl threonine	C5H11NO3	133.15	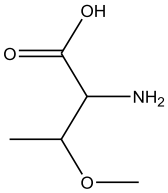
1.919	1.27	1,2,3,4-Tridecanetetrol	C13H28O4	248.36	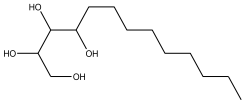
2.371	5.91	N-.alpha.-Acetylglycinamide	C4H8N2O2	116.12	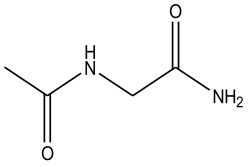
2.880	3.30	1H-Pyrazole-1-acetamide	C5H7N3O	125.13	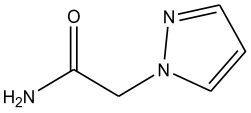
2.880	3.30	2-Myristynoyl-glycinamide	$C_{16}H_{28}N_2O_2$	280.41	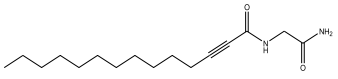
7.349	5.63	Azulene	$C_{10}H_8$	128.169	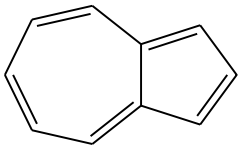
8.894	6.66	Eugenol	C10H12O2	164.2	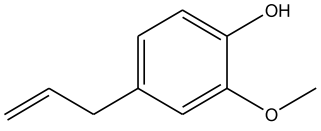
10.193	1.24	2,4-Di-tert-butylphenol	C14H22O	206.32	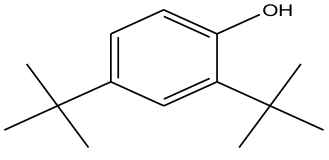

(*continued on next page*)

Table 1 (*continued*)

Retention Time	% area of peak	Molecule	Molecular Formula	Molecular weight ($g \times mol^{-1}$)	structure
13.752	2.20	Indazol-4-one	C7H4N2O	132.12	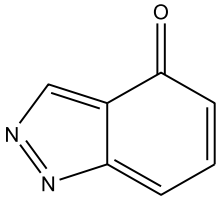
21.070	1.43	1,3-Benzenedicarboxylic acid	C8H6O4	166.13	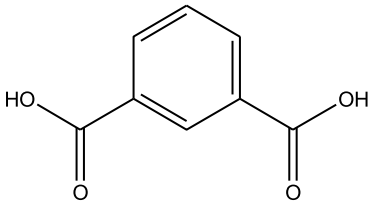
LC-MS analysis					
18.164		Quercetin-3-O-sophoroside	C27H30O17	626.5	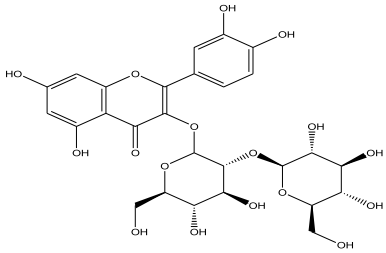
14.678		Esculin	C15H16O9	340.28	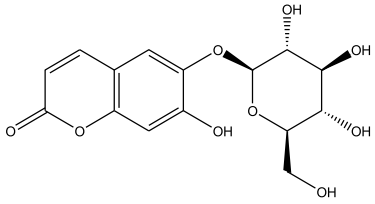
13.399		Guanosine	C10H13N5O5	283.24	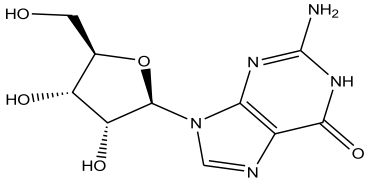
22.776		Linamarin	C10H17NO6	247.24	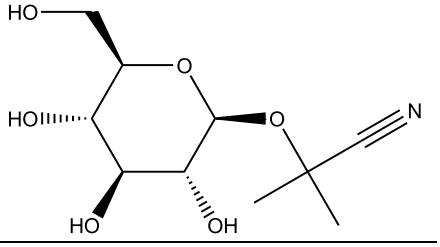

may function as a potent inhibitor with a strong potential for drug development, particularly in targeting specific active-site residues to maximize binding affinity and selectivity Figs. 6(a)–(d). The analysis of the 4XUM_135,398,635 complex involved a molecular dynamics simulation to examine the stability and binding interactions of the ligand within the protein's active site. Root Mean Square Deviation (RMSD) values indicate that both the protein and ligand maintain stable conformations throughout the 100-nanosecond simulation, suggesting that the ligand remains firmly anchored within the binding pocket. Root Mean Square Fluctuation (RMSF) data highlight minimal fluctuations in key binding site residues, further indicating stability and strong binding interactions. The ligand forms multiple hydrogen bonds with residues such as Cys285 and His323, which are essential for stabilizing its position. Additionally, hydrophobic contacts with residues like Leu330 and Met364 contribute to the ligand's affinity for the protein, providing a supportive environment within the pocket. Secondary structure analysis shows that the protein retains a stable configuration, with consistent alpha-helical and beta-strand regions throughout the simulation. Ligand properties, including its radius of gyration and polar surface area, suggest a compact and solvent-accessible conformation favorable for biological activity. Overall, this simulation supports the potential efficacy of the ligand as a selective inhibitor, with strong and consistent

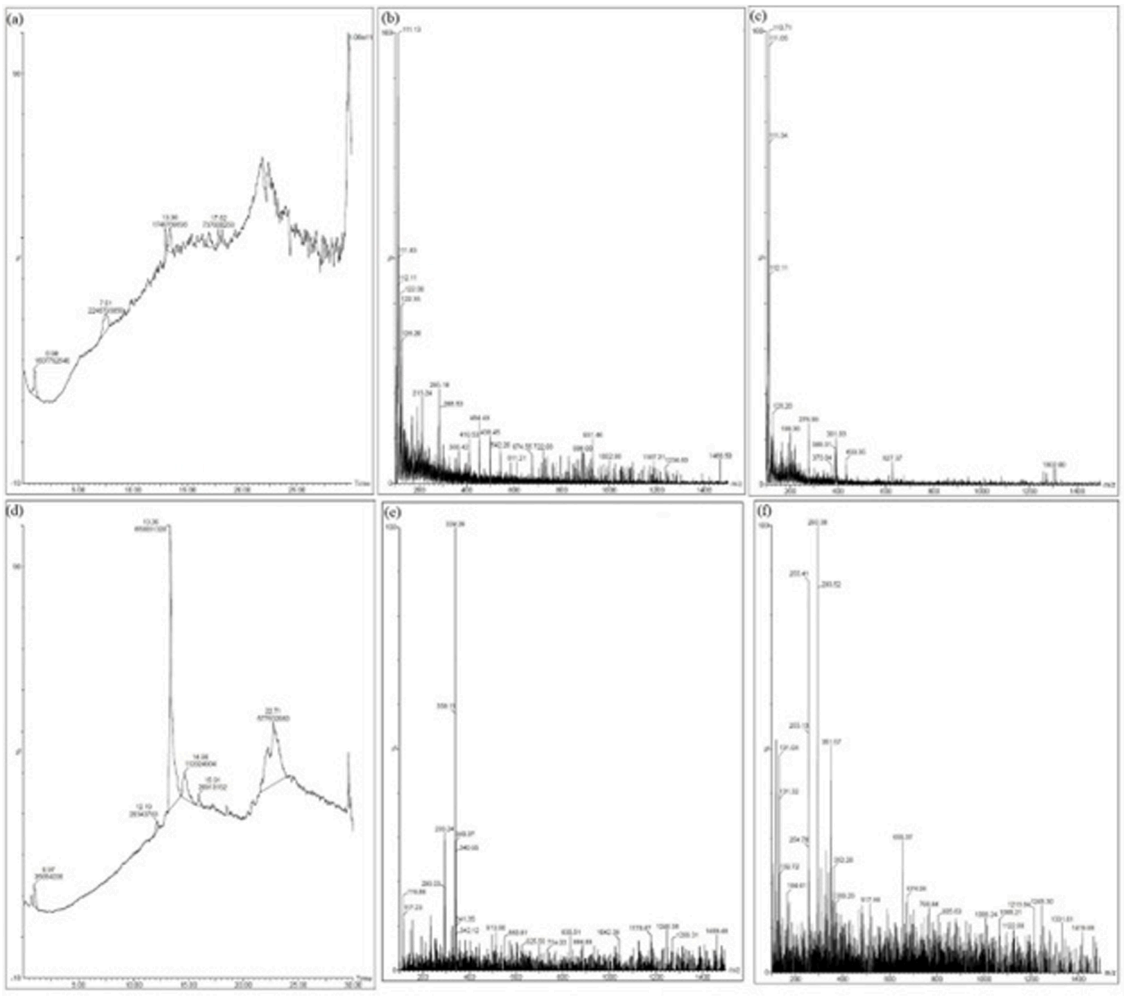

Fig. 4. LC-MS spectra of ethyl acetate fraction of endophytic fungal extract. Positive mode (a), Guanosine (b), Quercetin-3-O-sophoroside (c), Negative mode (d), Esculin (e), and Linamarin (f).

Table 2
Active molecules found in endophytic fungus and their binding affinity against PPARγ protein.

Molecule	Molecule id	Binding energy (kcal × mol^{-1})
ZINC5672437 (reference drug)	4829	−8.8
Quercetin-3-O-sophoroside	5282,166	−8.6
Esculin	5281,417	−8.5
2-Phenylpyrido[3,4-d]−1,3-oxazin-4-one	555,390	−7.8
Guanosine	135,398,635	−7.6
2,4-Di-tert-butylphenol	7311	−6.6
2-Myristynoyl-glycinamide	610,025	−6.4
Linamarin	11,128	−6.4
1,3-Benzenedicarboxylic_acid	8496	−6.2
Azulene	9231	−6.1
Eugenol	3314	−5.8
Indazol-4-one	20,146,588	−5.7
1,2,3,4-Tridecanetetrol	554,092	−5.5
1H-Pyrazole-1-acetamide	14,028,978	−5.0
dl-Erythro-O-methylthreonine	222,906	−4.7
N-.alpha.-Acetylglycinamide	28,326	−4.7
Pentanamide	12,298	−4.5
1H-Imidazole	795	−3.4

interactions that may enhance its inhibitory properties against the protein target Figs. 6(e)–(g). The analysis of the 4XUM_5,282,166 complex involved a detailed molecular dynamics simulation to evaluate the ligand's stability and interaction profile within the protein's binding pocket. RMSD analysis reveals that both protein and ligand exhibit stable conformations throughout the 100-nanosecond simulation, suggesting that the ligand is well-retained within the binding site. RMSF data highlight minimal fluctuations in binding site residues, confirming the robustness of the interactions. The ligand interacts through multiple hydrogen bonds with residues such as Glu343 and Ser342, stabilizing its position within the pocket. These hydrogen bonds are complemented by hydrophobic interactions with key residues like Tyr280 and Phe297, enhancing ligand affinity and stability. Secondary structure analysis demonstrates the protein's resilience, with alpha-helices and beta-strands remaining intact, supporting a stable binding environment. Ligand properties, including radius of gyration and solvent-accessible surface area, confirm a compact conformation that minimizes solvent exposure, which could enhance bioavailability. Additionally, the ligand torsion profile indicates limited rotational flexibility, reinforcing the ligand's structural stability in the pocket. Overall, the simulation findings highlight this ligand's potential as a potent and selective inhibitor, with promising interactions that suggest its effectiveness as a therapeutic agent Figs. 6(h)–(l). The molecular dynamics simulation of the 4XUM_5,281,417 complex evaluates the binding stability and interaction dynamics between the ligand and protein over a 100-nanosecond timeframe. RMSD analysis reveals that both the protein and ligand maintain a stable trajectory, indicative of a steady binding state with no significant conformational drift. RMSF results highlight minimal fluctuations, especially in key active site residues, suggesting a stable

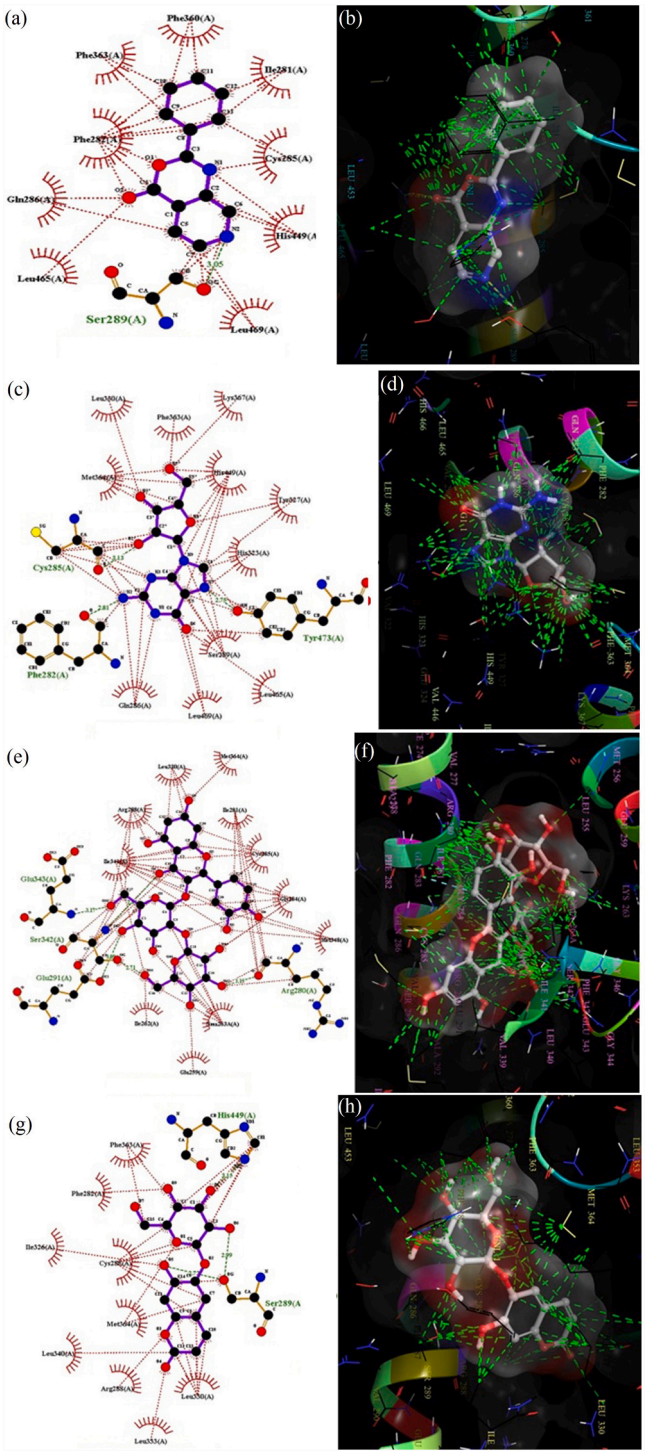

Fig. 5. Molecular docking analysis showcasing the interaction between 4XUM protein-ligand complexes with various compounds. Each subfigure highlights the binding poses, molecular interactions, and hydrogen bonding networks that stabilize the complexes. **(a, b)**: Visualization of the interaction between 4XUM and compound **555,390**. Panel **(a)** presents a 2D interaction diagram depicting hydrogen bonds, hydrophobic contacts, and π-π stacking interactions with surrounding amino acid residues, including Ser289(A), Phe366(A), and Leu405(A). Panel **(b)** illustrates the 3D binding pose of the ligand within the active site, showing surface complementarity and interaction networks. **(c, d)**: Docking results for compound **135,398,635** with 4XUM. Panel **(c)** demonstrates the 2D interaction map, highlighting key residues such as Met365(A), Tyr326(A), and Cys288(A) forming critical contacts with the ligand. Panel **(d)** displays the 3D docking orientation, emphasizing hydrogen bonding and hydrophobic environment stabilization. (e, f)**:** Interaction analysis for compound **5282,166** bound to 4XUM. The 2D schematic in **(e)** outlines significant bonds and residues, including Glu384(A), Ser289(A), and Tyr407(A). Panel (f) captures the 3D structural alignment of the ligand in the binding pocket. (g, h): Binding profile of compound **5281,417** with 4XUM. Panel (g) features a 2D interaction diagram, with residues like His404(A), Leu405(A), and Asp406(A) contributing to ligand stability. Panel **(h)** highlights the 3D binding pose, showing molecular surface interactions and the ligand's placement within the binding site.

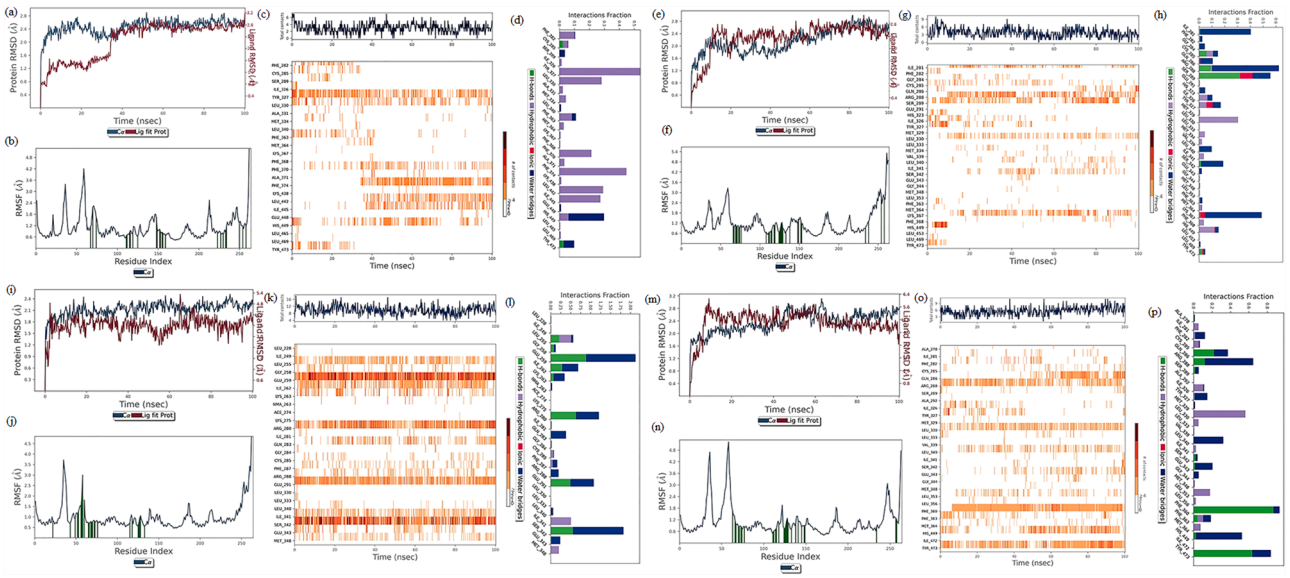

Fig. 6. (a) shows the RMSD of protein and ligand over 100 ns, indicating stability. (b) presents the RMSF values per residue, highlighting flexible regions. (c) displays residue-ligand contacts over time, while (d) quantifies interaction types, emphasizing dominant hydrophobic and hydrogen bonds with key residues like Phe370, Leu330, and Tyr473. (e) depicts protein and ligand RMSD over 100 ns, showing system stability. (f) shows RMSF values, identifying flexible residues. (g) illustrates residue-ligand contact frequency, while (h) categorizes interaction types, highlighting significant hydrogen bonding and hydrophobic interactions with Ser289, Glu343, and His449. (i) illustrates protein and ligand RMSD over 100 ns, showing complex stability. (j) displays RMSF, highlighting flexible residues. (k) depicts residue-ligand contact frequencies, and (l) shows interaction types, emphasizing hydrogen bonds and hydrophobic interactions with key residues such as Glu259, Arg280, and Ser342. (m) shows protein and ligand RMSD over 100 ns, demonstrating structural stability. (n) presents RMSF, identifying flexible residues. (o) visualizes residue-ligand contact frequencies, and (p) displays interaction types, highlighting hydrogen bonds, hydrophobic contacts, and water bridges with key residues like Arg286, Ser289, and Phe360.

interaction environment. Key interactions include multiple hydrogen bonds, particularly with residues Ser289 and Glu343, which stabilize the ligand within the pocket. These bonds are complemented by hydrophobic contacts with residues like Phe363 and Leu469, enhancing the ligand's retention and positioning within the binding site. Secondary structure analysis shows consistent alpha-helix and beta-strand presence, further supporting a stable interaction framework around the ligand. The ligand's compact conformation is confirmed by the radius of gyration and solvent-accessible surface area values, which suggest limited solvent exposure is an advantageous feature for bioavailability. Additionally, the torsion profile of the ligand shows minimal flexibility, reinforcing the likelihood of a locked-in binding conformation. Overall, this simulation provides evidence for the ligand's potential as a potent and selective inhibitor with promising affinity and stability for therapeutic applications Figs. 6(m)–(p).

3.6. Density functional theory (DFT)

The link between geometry and electronic characteristics of molecules was investigated by a computational examination of density functional theory (DFT) studies. The ability of a molecule to give electrons is fundamentally indicated by its highest occupied molecular orbital (HOMO). The primary determinants of a molecule's biological effects are its lowest unoccupied molecular orbital (LUMO) and highest occupied molecular orbital (HOMO). The HONO-LUMO energy gaps were assessed using the B3LYP level with the 6–311 G (d, p) basis set for the top four compounds (Phenylpyrido[3,4-d]−1,3-oxazin-4-one, Guanosine Quercetin-3-O-sophoroside, and Esculin, 2-) from endophytic fungus and reference drug (ZINC5672437). The diagram of HOMO-LUMO is shown in Table 3. The HOMO–LUMO energy gap of the reference drug (ZINC5672437) was 0.7688, whereas the greatest energy gap molecule was Guanosine at 4.1933, followed by 2-Phenylpyrido [3,4-d]−1,3-oxazin-4-one at 3.3524, Quercetin-3-O-sophoroside at 3.1962, and Esculin at 2.8280. The energy gap measurement shows that the four chosen molecules are all incredibly stable.

3.7. DPPH radicals scavenging assay

Fig. 7(a) displayed the DPPH-radicals scavenging ability of varied concentrations of endophytic fungal (*Penicillium oxalicum*) extract. The graph showed that concentration-dependent scavenging potentials of endophytic fungal extract were observed. 150, 100, 50, 20 and 10 μg × mL^{-1} of *Penicillium oxalicum* extract showed 71.88 ± 1.542 %, 65.56 ± 1.535 %, 52.907 ± 1.557 %, 42.657 ± 1.53 % 32.29 ± 2.02 %, respectively. While 100 μg × mL^{-1} of rutin scavenged 70.627 ± 1.015 % DPPH radicals. IC_{50} concentration of endophytic fungal (*Penicillium oxalicum*) extract was 55.72 μg × mL^{-1}.

3.8. ABTS radicals scavenging potentials

The varied ethyl acetate endophytic fungal extract concentrations showed a concentration-based de-colorization of ABTS radical solution. 10 μg × mL^{-1} of extract de-colorize 32.98 ± 1.535 % of free radicals. Fig. 7(b) illustrates the scavenging potential of various concentrations of endophytic fungal extracts on ABTS radicals. IC_{50} concentration of endophytic fungal (*Penicillium oxalicum*) extract was 55.68 μg × mL^{-1}.

3.9. FRAP assay

Fig. 7(c) demonstrates the ability of different concentrations of the ethyl acetate fraction of Penicillium oxalicum to reduce ferric ions. The highest reduction power, as determined by the FRAP assay, was observed at a concentration of 150 μg × mL^{-1} of the Penicillium oxalicum extract, with a value of 67.623 ± 1.015 %. The IC50 concentration of the endophytic fungal (Penicillium oxalicum) extract was 79.54 μg × mL^{-1}. Fig. 7(c) displays the ferric-reducing potential of various concentrations of endophytic fungal extracts.

Table 3
E_{HOMO} and E_{LUMO} and ΔeV values of selected top binding scored active compounds and reference drug ZINC5672437.

Molecule	HOMO	E_{HOMO}	LUMO	E_{LUMO}	Energy gap (ΔeV)
Quercetin-3-O-sophoroside	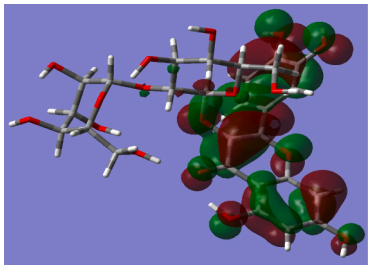	−8.6526	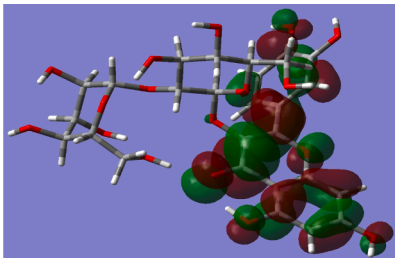	−5.4564	3.1962
Esculin	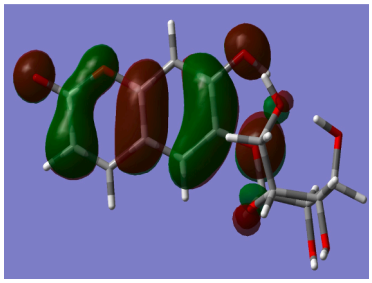	−8.9442	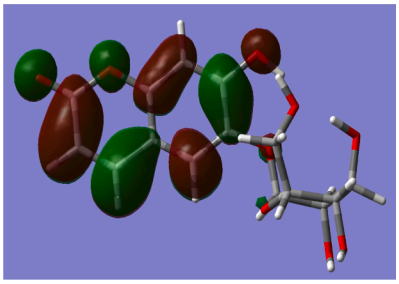	−5.6711	2.8280
2-Phenylpyrido[3,4-d]−1,3-oxazin-4-one	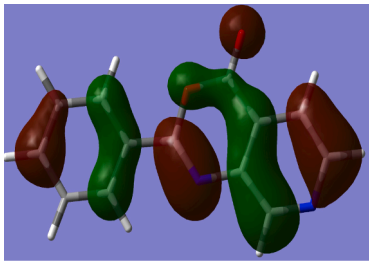	−9.1843	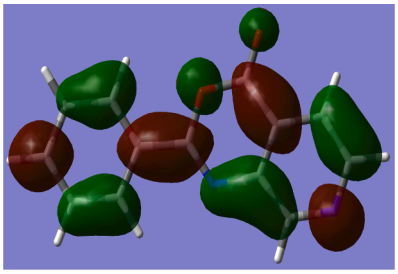	−5.8319	3.3524
Guanosine	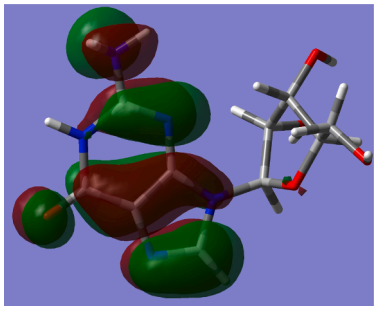	−8.3000	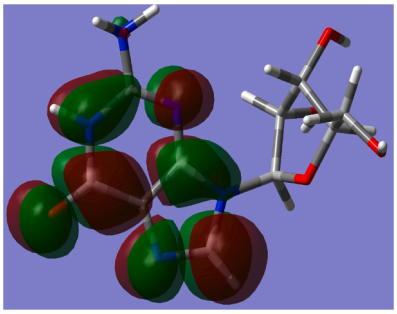	−4.1067	4.1932
ZINC5672437	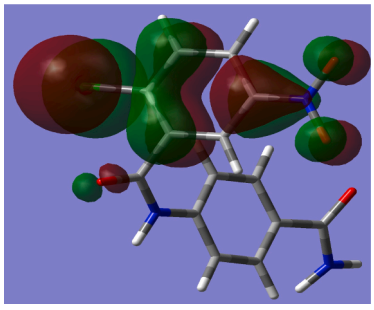	−2.665	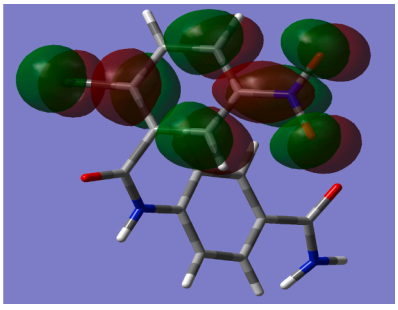	−1.8969	0.7687

3.10. Non-cellular antidiabetic activity

3.10.1. α-amylase inhibitory activity

Endophytic fungi, *Penicillium oxalicum* extract at a concentration of 10, 25, 50 100, 150 μg × mL^{-1} showed 21.14 ± 1.02 %, 23.983 ± 1.564 %, 34.717 ± 1.553 %, 46.82 ± 1.552 %, 50.18 ± 0.951 % respectively, inhibitory effects of α-amylase activity with an IC_{50} value 133.86 μg × mL^{-1}. At the same time, 100 μg × mL^{-1} of pioglitazone showed 77.367 ± 1.025 % of α-amylase inhibitory activity. Fig. 8(a) illustrates the α-amylase inhibitory activity of various concentrations of *Penicillium*

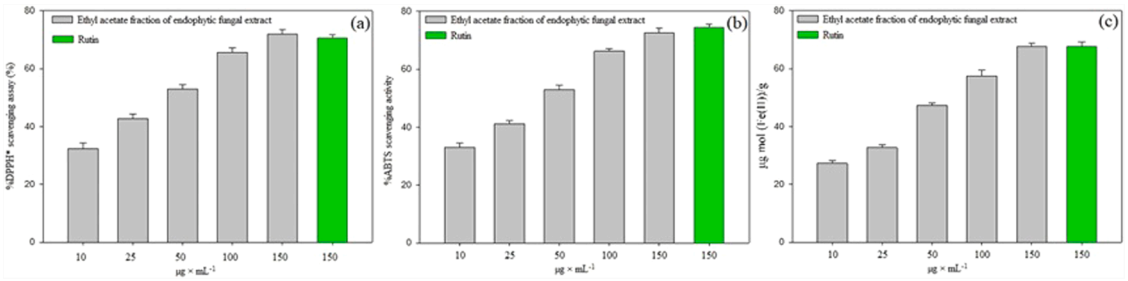

Fig. 7. DPPH radical scavenging activities of various concentrations of endophytic fungal extract (a); ABTS radical scavenging activities of various concentrations of endophytic fungal extract (b); FRAP potentials of various concentrations of endophytic fungal extract (c).

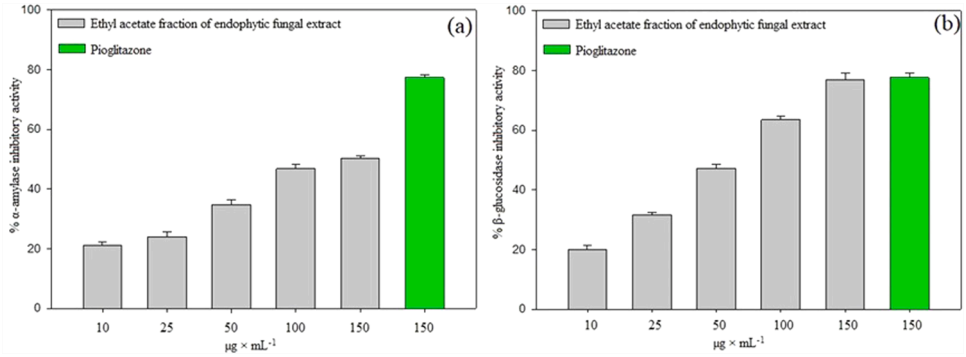

Fig. 8. α-amylase enzyme inhibitory activity of various concentrations of endophytic fungal extract (a), β-glucosidase enzyme inhibitory activity of various concentrations of endophytic fungal extract (b).

oxalicum extract.

3.10.2. β-glucosidase inhibitory activity

Endophytic fungal extract at a concentration of 100 μg × mL^{-1} showed 63.443 ± 1.104 % of inhibitory activity of β-glucosidase with an IC_{50} value of 72.63 μg × mL^{-1}. At the same time, 100 μg × mL^{-1} of pioglitazone showed 77.367 ± 1.52 % of β-glucosidase inhibitory activity. Fig. 8(b) shows the β-glucosidase inhibitory activity of various concentrations of endophytic fungal extracts.

4. Discussion

This study aimed to screen and identify potential antioxidant and antidiabetic molecules from endophytic fungi isolated from medicinal plants. Endophytic fungi can develop the same active molecules as their host plant, opening new avenues for natural small-molecule research [44]. Endophytic fungi are novel sources of a diversified group of molecules that have potential applications in the field of pharmaceutical, food, and agricultural sectors [45]. These fungi generate a broad range of secondary metabolites belonging to the group of alkaloids, glycosides, terpenoids, peptides, and other structural diversified molecules [46]. Currently used, many of the drugs are derived from natural sources, like plants and microorganisms. For example, (*S*)-(+)−2-cis-4-trans-abscisic acid, 7′-hydroxy-abscisic acid, and 4-des-hydroxyl altersolanol A, Methyl-5-docosenoate, (+)-epicoccone C, (-)-epicoccone C, epicoccone D, epicoccone E, epicolactone A, flavimycins A, epicocconigrone A, etc. [47,48]. The research reported that metabolic profiling of ethyl acetate extract (EAE) of endophytic fungus *Penicillium campo notum (PC) and Penicillium fuscoglaucum (PF)*, revealed the presence of phytochemicals, including pnictide B, p-hydroxyphenyl anarrisate, and dihydroxy stearic acid. these compounds exhibited substantial interactions with human cancer-related proteins such as epidermal growth factor receptor (EGFR), N-myristoyltransferase isoform 2 (NMT-2), cyclin-dependent kinase 2 (CDK-2), and c-mesenchymal epithelial transition factor kinase (c-Met K) evidenced by in-silico molecular docking analysis [49]. Endophytic fungi have several advantages, including being renewable, widely available, inexpensive, and ecologically friendly sources of bioactive compounds [50]. This study isolated *Penicillium oxalicum* endophytic fungus from the tuberous root of cassava. Further, the ethyl acetate fraction of *P. oxalicum* fungal extract showed significant antioxidant, α-amylase, and β-glucosidase enzyme inhibitory actions. The results of these antioxidant and enzymatic inhibitory activities are responsible for the possession of bioactive molecules produced by endophytic fungus. In addition, seventeen bioactive molecules were identified through GC–MS and LC-MS from the ethyl acetate fraction of endophytic fungus.

The extraction method and solvent selection may enhance the yield of bioactive molecules from endophytic fungi. This study used an ultrasound-aided extraction technique with ethyl acetate as an extracting solvent to extract maximum bioactive molecules from endophytic fungi, *P. oxalicum.* Ultrasound-assisted extraction is a highly considered technology for extraction due to its ability to employ smaller amounts of solvents, lower temperatures for automation, reduced energy requirements, and maximum yield [51]. Additionally, the extraction process for bioactive molecules and heat-sensitive compounds from the source is more efficient in terms of time. Ultrasonic vibrations expedite the extraction of components by increasing mass movement into the solvent. In addition, they induce the rupture of the fungal cell membrane by applying physical pressure during ultrasound cavitation [52].

Further, the volatile and non-volatile nature of the bioactive molecules present in the ethyl acetate fraction of *P. oxalicum* were identified using GC–MS and LC-MS, respectively. The GC–MS spectrum of the ethyl acetate fraction of *P. oxalicum* showed seventeen peaks and thirteen active molecules were determined based on the nuclear structure of the seventeen peaks. Similarly, in our previous work, thirteen peaks were observed from the ethyl acetate fraction of endophytic fungi *Curvularia geniculata* L. from *Phyllanthus niruri* L. One of the bioactive molecules, quercetin-3-O-sophoroside, was isolated from Hibiscus rosa-sinensis Linn. for the first time. The molecule possesses neuroprotective effects against scopolamine-induced amnesia. Another molecule, esculin (40

mg × kg^{-1}), reduces insulin resistance and enhances glutathione peroxidase, superoxide dismutase, and catalase activity in the pancreas and liver of diabetic mice [53]. Esculin has been reported to alleviate diabetic neuropathy in experimental diabetic rats [54]. Further, Guanosine is a purine nucleoside believed to have neuroprotective effects. It is secreted in the brain physiologically and after pathological events, lowering neuroinflammation, oxidative stress, and excitotoxicity while having trophic effects on neuronal and glial cells [55].

In silico molecular modeling studies are helpful for discovering highly effective molecules from a compound library, while also reducing design and synthetic research effects [56]. Bioinformatic analysis can aid in identifying, screening, and refining therapeutic targets, as well as predicting toxic effects and drug resistance [57]. The present study identified seventeen molecules from an endophytic fungus, which are docked against one of the diabetic receptors, PPARγ. It compared them with ZINC5672437 (co-crystalized ligand in the target protein PPARγ). Binding energy of 2-Phenylpyrido[3,4-d]−1,3-oxazin-4-one (CID: 555, 390) −9.40 kcal × mol^{-1}, Guanosine (CID: 135,398,635) −7.60 kcal × mol^{-1}, Quercetin-3-O-sophoroside (CID: 5282,166) −7.60 kcal × mol^{-1}, and Esculin (CID: 5281,417) −7.20 kcal × mol^{-1} are top scored and near to reference drug, ZINC5672437 (−8.80 kcal × mol^{-1}). This was followed by the molecular dynamic simulation studies of top-scored molecules, except Guanosine and the other three molecules have low stability with the target protein, PPARγ. Similarly, bioactive volatile compounds such as γ-terpinene, 4-carvomenthenol, heneicosane, and 2, 5-piperazine-dione identified from endophytic fungus (*Paraconiothyrium. brasiliense* MT269522) were isolated from the fruit of *Capsicum annum* L. further; molecular docking analysis confirmed 2, 5-piperazine-dione had considerable interaction with DHPS (Dihydropteroate Synthase) enzyme thereby induced antibacterial activity like sulfonamide class of antibiotic [58]

It has been observed that free radicals play a significant role in many diseases, including cancer, diabetes mellitus, Alzheimer's, Parkinson's, and arthritis. Overproduction of free radicals can have various detrimental effects on the biological system [59]. Chronic hyperglycaemia is the primary cause of the majority of diabetes-related long-term issues [60]. Protein glycation, a primary source of free radicals, is brought on by hyperglycaemia [61]. Research indicates that free radicals play a critical role in the onset and consequences of diabetes. Changes in kidney, nerve, vascular tissue, foot ulceration, and metabolism are among these effects [62]. In this study, varied concentrations of ethyl acetate fraction of endophytic fungal extract demonstrated excellent free radicals (DPPH* and ABTS*) scavenging potential and ferric-reducing power. 100 μg × mL^{-1} of endophytic fungal extract displayed 65.56 ± 1.535 % DPPH* scavenging, 66.17 ± 1.01 % ABTS* scavenging and 57.43 ± 2.02 % FRAP abilities. Similarly, the endophytic fungi BvFV and BvFIX isolated from leaves of *Bauhinia variegate*, the methanolic extract of BvFIX showed the lowest IC_{50} value (12.09 mg × mL^{-1}) of DPPH* scavenging assay [63].

Delaying the activity of α-amylase and β-glucosidase enzymes in the intestine may delay the absorption of ingested carbs and reduce hyperglycaemic episodes [64]. Endophytic fungus active compounds effectively inhibit α-amylase and β-glucosidase enzymes, reducing insulin peaks in diabetes mellitus. Inhibition of both enzymes should reduce postprandial hyperglycaemia, which could be a useful method for diabetes management. In this study, ethyl acetate fraction of *P. oxalicum* fungal extract demonstrated good α-amylase and β-glucosidase enzymes inhibitory potentials of IC_{50} values of 133.86 μg × mL^{-1} and 72.63 μg × mL^{-1}, respectively. Similarly, compounds of rostratazine B and exserohilone isolated from the endophytic fungus *Setosphaeria rostrata* isolated from the medicinal plant *Costus speciosus* showed excellent alpha-glucosidase inhibitory activity and porcine pancreatic alpha-amylase inhibitory activity, respectively [65].

5. Conclusions

The bioassay-directed fraction of endophytic fungi extract from *P. oxalicum* was examined for the bioactive molecules through GC–MS and LC-MS analysis, whereby thirteen and four molecules (a total of seventeen), respectively, were identified. Among them, four molecules 2-Phenylpyrido[3,4-d]−1,3-oxazin-4-one, Guanosine, Quercetin-3-O-sophoroside, Esculin, displayed a better binding affinity with the target protein, PPARγ protein. Further, the molecular dynamics simulation studies revealed Guanosine-PPARγ protein complex showed strong intermolecular interactions and stability. The results of the antioxidant assay demonstrated that the ethyl acetate fraction of endophytic fungi showed significant free radical scavenging and ferric ion-reducing potentials. IC_{50} values of DPPH*, ABTS* scavenging and FRAP were 55.72, 55.68 and 79.54 μg × mL^{-1}, respectively. On the other side, α-amylase and β-glucosidase inhibitory assay of ethyl acetate fraction of endophytic fungal extract showed better inhibitory activity and IC_{50} values of 133.86 and 72.63 μg × mL^{-1}. *P. oxalicum*, a possible endophytic fungal found in Cassava tuberous root, may act as an antioxidant and antidiabetic molecule. However, the next step will require in vitro cellular and in vivo animal research.

CRediT authorship contribution statement

Keerthana Nagarajan: Writing – review & editing, Visualization, Validation, Conceptualization. **Mahisha Devi Chelladurai:** Writing – review & editing, Visualization, Validation, Conceptualization. **Sivaranjini Mani:** Visualization, Validation, Formal analysis. **Parasuraman Pavadai:** Visualization, Validation, Software, Formal analysis. **Panneerselvam Theivendren:** Writing – review & editing, Writing – original draft, Software, Methodology. **Ponnusamy Palanisamy:** Visualization, Validation, Supervision, Formal analysis. **Murugesan Sankaranarayanan:** Visualization, Validation, Supervision, Formal analysis. **Selvaraj Kunjiappan:** Writing – review & editing, Writing – original draft, Methodology, Conceptualization.

Declaration of competing interest

The authors declare that they have no known competing financial interests or personal relationships that could have appeared to influence the work reported in this paper.

Acknowledgements

The authors thank the Management of Kalasalingam Academy of Research and Education, Krishnankoil, Tamil Nadu, India, for providing all required research facilities. SK gratefully acknowledge the Management of Kalasalingam Academy of Research and Education for the Seed Money Grant (KARE/VC/R&D/SMPG/2021–2022/1).

Supplementary materials

Supplementary material associated with this article can be found, in the online version, at doi:10.1016/j.molstruc.2025.142083.

Data availability

No data was used for the research described in the article.

References

[1] Y. Mukhtar, A. Galalain, U. Yunusa, A modern overview on diabetes mellitus: a chronic endocrine disorder, Eur. J. Biol. 5 (2) (2020) 1–14.
[2] B.K. Tripathi, A.K. Srivastava, Diabetes mellitus: complications and therapeutics, Med. Sci. Monit. 12 (7) (2006) 130–147.
[3] S. Kunjiappan, T. Panneerselvam, P. Prasad, S. Sukumaran, B. Somasundaram, M. Sankaranarayanan, I. Murugan, P. Parasuraman, Design, graph theoretical

analysis and in silico modeling of Dunaliella bardawil biomass encapsulated keratin nanoparticles: a scaffold for effective glucose utilization, Biomed. Mater. 13 (4) (2018) 045012.
[4] C. Palanichamy, D. Nayak Ammunje, P. Pavadai, S. Ram Kumar Pandian, P. Theivendren, S.J. Kabilan, E. Babkiewicz, P. Maszczyk, S. Kunjiappan, Mimosa pudica Linn. Extract improves aphrodisiac performance in diabetes-induced male Wister rats, J. Biomol. Struct. Dyn. (2023) 1–20.
[5] U. Galicia-Garcia, A. Benito-Vicente, S. Jebari, A. Larrea-Sebal, H. Siddiqi, K. B. Uribe, H. Ostolaza, C. Martín, Pathophysiology of type 2 diabetes mellitus, Int. J. Mol. Sci. 21 (17) (2020) 6275.
[6] I. Belhadj Slimen, T. Najar, A. Ghram, H. Dabbebi, M. Ben Mrad, M. Abdrabbah, Reactive oxygen species, heat stress and oxidative-induced mitochondrial damage. A review, Int. J. Hyperth. 30 (7) (2014) 513–523.
[7] M.E. Cerf, Beta cell dysfunction and insulin resistance, Front. Endocrinol. (Lausanne) 4 (2013) 37.
[8] N. Katakami, Mechanism of development of atherosclerosis and cardiovascular disease in diabetes mellitus, J. Atheroscler. Thromb. 25 (1) (2018) 27–39.
[9] D. Soumya, B. Srilatha, Late stage complications of diabetes and insulin resistance, J. Diabetes. Metab. 2 (9) (2011) 1000167.
[10] F. Khoder-Agha, T. Kietzmann, The glyco-redox interplay: principles and consequences on the role of reactive oxygen species during protein glycosylation, Redox. Biol. 42 (2021) 101888.
[11] S.D. Clarke, P. Thuillier, R.A. Baillie, X. Sha, Peroxisome proliferator-activated receptors: a family of lipid-activated transcription factors, Am. J. Clin. Nutr. 70 (4) (1999) 566–571.
[12] I. Bravo-Ruiz, M.Á. Medina, B. Martínez-Poveda, From food to genes: transcriptional regulation of metabolism by lipids and carbohydrates, Nutrients. 13 (5) (2021) 1513.
[13] X. Shao, M. Wang, X. Wei, S. Deng, N. Fu, Q. Peng, Y. Jiang, L. Ye, J. Xie, Y. Lin, Peroxisome proliferator-activated receptor-γ: master regulator of adipogenesis and obesity, Curr. Stem Cell Res. Ther. 11 (3) (2016) 282–289.
[14] M.A. Davidson, A pharmacovigilance approach for assessing cardiovascular, osteological, and carcinogenic risk associated with thiazolidinedione drugs used in the treatment of type 2 diabetes mellitus, Université d'Ottawa/University of Ottawa, 2018.
[15] S. Tiwari, P. Kaur, D. Gupta, S. Chaudhury, M. Chaudhary, A. Mittal, S. Kumar, S. K. Sahu, An insight into the development of potential antidiabetic agents along with their therapeutic targets, Endocr. Metab. Immune Disord. Drug Targets (Formerly Current Drug Targets-Immune, Endocrine & Metabolic Disorders) 24 (1) (2024) 50–85.
[16] W. Ahsan, The journey of thiazolidinediones as modulators of PPARs for the management of diabetes: a current perspective, Curr. Pharm. Des. 25 (23) (2019) 2540–2554.
[17] F. Ovalle, J.F. Ovalle-Berúmen, Thiazolidinediones: a review of their benefits and risks, South. Med. J. 95 (10) (2002) 1188–1194.
[18] M.A. Davidson, D.R. Mattison, L. Azoulay, D. Krewski, Thiazolidinedione drugs in the treatment of type 2 diabetes mellitus: past, present and future, Crit. Rev. Toxicol. 48 (1) (2018) 52–108.
[19] D. Alemán-González-Duhart, F. Tamay-Cach, S. Álvarez-Almazán, J. Mendieta-Wejebe, Current advances in the biochemical and physiological aspects of the treatment of type 2 diabetes mellitus with thiazolidinediones, PPAR. Res. 2016 (2016).
[20] J.E. Calfee, Avandia and FDA Regulation, FDLI Update (2010) 27.
[21] J. Guimarães, Diabetes-old therapies revisited, Endocrinol Metab. Int. J. 3 (4) (2016) 00056.
[22] S.R.N.S.P. Mohidin, S. Moshawih, A. Hermansyah, M.I. Asmuni, N. Shafqat, L. C. Ming, Cassava (Manihot esculenta Crantz): a systematic review for the pharmacological activities, traditional uses, nutritional values, and phytochemistry, J. Evid. Based. Integr. Med. 28 (2023), 2515690 × 231206227.
[23] A. Chandrasekara, T.Josheph Kumar, Roots and tuber crops as functional foods: a review on phytochemical constituents and their potential health benefits, Int. J. Food Sci. 2016 (2016).
[24] L. Ciumărnean, M.V. Milaciu, O. Runcan, Ş.C. Vesa, A.L. Răchişan, V. Negrean, M.-G. Perné, V.I. Donca, T.-G. Alexescu, I. Para, The effects of flavonoids in cardiovascular diseases, Molecules 25 (18) (2020) 4320.
[25] A.K. Kalimuthu, P. Pavadai, T. Panneerselvam, E. Babkiewicz, J. Pijanowska, P. Mrówka, G. Rajagopal, V. Deepak, K. Sundar, P. Maszczyk, Cytotoxic potential of bioactive compounds from Aspergillus flavus, an endophytic fungus isolated from Cynodon dactylon, against breast cancer: experimental and computational approach, Molecules 27 (24) (2022) 8814.
[26] A. Singh, D.K. Singh, R.N. Kharwar, J.F. White, S.K. Gond, Fungal endophytes as efficient sources of plant-derived bioactive compounds and their prospective applications in natural product drug discovery: insights, avenues, and challenges, Microorganisms 9 (1) (2021) 197.
[27] V.K. Singh, A. Kumar, Secondary metabolites from endophytic fungi: production, methods of analysis, and diverse pharmaceutical potential, Symbiosis 90 (2) (2023) 111–125.
[28] A.K. Kalimuthu, P. Parasuraman, P. Sivakumar, S. Murugesan, S. Arunachalam, S. R.K. Pandian, V. Ravishankar, D.N. Ammunje, M. Sampath, T. Panneerselvam, In silico, in vitro screening of antioxidant and anticancer potentials of bioactive secondary metabolites from an endophytic fungus (Curvularia sp.) from Phyllanthus niruri L, Environ. Sci. Pollut. Res. 29 (32) (2022) 48908–48925.
[29] S. Mollaei, O. Khanehbarndaz, Z. Gerami-Khashal, M. Ebadi, Molecular identification and phytochemical screening of endophytic fungi isolated from lithospermum officinale L. roots: a new source of shikonin, Phytochemistry 168 (2019) 112116.
[30] K. Selvaraj, P. Theivendren, P. Pavadai, V. Ravishankar, P. Palanisamy, M. Gopal, S.R. Dharmalingam, M. Sankaranarayanan, Impact of physicochemical parameters on effective extraction of bioactive compounds from natural sources: an overview, Curr. Bioact. Compd. 18 (4) (2022) 11–27.
[31] D.J.P. Daniel, S. Shanmugasundaram, K.S. Chandra Mohan, V. Siva Bharathi, J. K. Abraham, P. Anbazhagan, P. Pavadai, S. Ram Kumar Pandian, K. Sundar, S. Kunjiappan, Elucidating the role of phytocompounds from Brassica oleracea var. Italic (Broccoli) on hyperthyroidism: an in-silico approach, In. Silico Pharmacol. 12 (1) (2024) 6.
[32] B. Doherty, X. Zhong, S. Gathiaka, B. Li, O. Acevedo, Revisiting OPLS force field parameters for ionic liquid simulations, J. Chem. Theory. Comput. 13 (12) (2017) 6131–6145.
[33] D.J. Price, C.L. Brooks III, A modified TIP3P water potential for simulation with Ewald summation, J. Chem. Phys. 121 (20) (2004) 10096–10103.
[34] H. Liu, Y. Shi, L. Huang, Deformation behaviors of a model metallic glass under 3-D nanoindentation studied in molecular dynamics simulation, J. Non-Cryst. Solids: X 16 (2022) 100130.
[35] P. Petchimuthu, C. Ala, S. Kunjiappan, P. Pavadai, M. Sankaranarayanan, S. Ram Kumar Pandian, K. Sundar, Pharmacoinformatics-based identification of phytochemicals from Solanum torvum Swartz. Fruits as potential inhibitors for MAPK14 protein, J. Biomol. Struct. Dyn. (2023) 1–17.
[36] S. Vellur, P. Pavadai, S.R.K. Pandian, C. Palanichamy, S.J. Kabilan, K. Sundar, S. Kannan, S. Kunjiappan, Optimization of ultrasound-assisted extraction of bioactive chemicals from Hemidesmus indicus (L.) R. Br. using response surface methodology and adaptive neuro-fuzzy inference system, Food Sci. Biotechnol. 33 (2) (2024) 327–341.
[37] İ. Gulcin, S.H. Alwasel, DPPH radical scavenging assay, Processes 11 (8) (2023) 2248.
[38] M. Govindappa, N. Bharath, H. Shruthi, G. Santoyo, In vitro antioxidant activity and phytochemical screening of endophytic extracts of *Crotalaria pallida*, Free Radicals and Antioxidants 1 (3) (2011) 79–86.
[39] N. Nenadis, L.-F. Wang, M. Tsimidou, H.-Y. Zhang, Estimation of scavenging activity of phenolic compounds using the ABTS•+ assay, J. Agric. Food Chem. 52 (15) (2004) 4669–4674.
[40] S. Kunjiappan, T. Panneerselvam, S. Kannan, B. Somasundaram, M. Sankaranarayanan, S. Arunachalam, A. Manimaran, Optimization of microwave-assisted extraction of bioactive compounds from Dunaliella bardawil using RSM and ANFIS modeling and assessment of the anticancer activity of bioactive compounds, Curr. Microw. Chem. 5 (2) (2018) 139–154.
[41] B. Ou, D. Huang, M. Hampsch-Woodill, J.A. Flanagan, E.K. Deemer, Analysis of antioxidant activities of common vegetables employing oxygen radical absorbance capacity (ORAC) and ferric reducing antioxidant power (FRAP) assays: a comparative study, J. Agric. Food Chem. 50 (11) (2002) 3122–3128.
[42] N. Pavithra, L. Sathish, N. Babu, V. Venkatarathanamma, H. Pushpalatha, G. B. Reddy, K. Ananda, Evaluation of α-amylase, α-glucosidase and aldose reductase inhibitors in ethyl acetate extracts of endophytic fungi isolated from antidiabetic medicinal plants, Int. J. Pharm. Sci. Res. 5 (12) (2014) 5334–5341.
[43] M.M.A.A. El-Gendy, S.M. Yahya, A.R. Hamed, M.M. Soltan, A.M.A. El-Bondkly, Phylogenetic analysis and biological evaluation of marine endophytic fungi derived from Red Sea sponge hyrtios erectus, Appl. Biochem. Biotechnol. 185 (2018) 755–777.
[44] P. Tiwari, H. Bae, Endophytic fungi: key insights, emerging prospects, and challenges in natural product drug discovery, Microorganisms 10 (2) (2022) 360.
[45] K.L. Rana, D. Kour, I. Sheikh, N. Yadav, A.N. Yadav, V. Kumar, B.P. Singh, H.S. Dhaliwal, A.K. Saxena, Biodiversity of endophytic fungi from diverse niches and their biotechnological applications, advances in endophytic fungal research: present status and future challenges (2019) 105–144.
[46] G.F. Bills, J.B. Gloer, Biologically active secondary metabolites from the fungi, Microbiol. Spectr. 4 (6) (2016), 10.1128/microbiolspec. funk-0009-2016.
[47] P.F. Uzor, P.O. Osadebe, N.J. Nwodo, Antidiabetic activity of extract and compounds from an endophytic fungus nigrospora oryzae, Drug Res. 67 (05) (2017) 308–311.
[48] M.S. Elnaggar, S. Fayez, A. Anwar, S.S. Ebada, Cytotoxic naphtho-and benzofurans from an endophytic fungus Epicoccum nigrum Ann-B-2 associated with Annona squamosa fruits, Sci. Rep. 14 (1) (2024) 4940.
[49] K.V. Naveen, S. Park, K. Saravanakumar, A. Sathiyaseelan, M.-H. Wang, Ultraperformance liquid chromatography-based metabolite profiling and cytotoxic activity of the ethyl acetate extract of two endophytic penicillium sp, Process Biochem. 130 (2023) 366–378.
[50] K.L. Rana, D. Kour, I. Sheikh, A. Dhiman, N. Yadav, A.N. Yadav, A.A. Rastegari, K. Singh, A.K. Saxena, Endophytic fungi: biodiversity, ecological significance, and potential industrial applications, Recent advancement in white biotechnology through fungi: volume 1, diversity and enzymes perspectives (2019) 1–62.
[51] S. Kunjiappan, L.K. Ramasamy, S. Kannan, P. Pavadai, P. Theivendren, P. Palanisamy, Optimization of ultrasound-aided extraction of bioactive ingredients from Vitis vinifera seeds using RSM and ANFIS modeling with machine learning algorithm, Sci. Rep. 14 (1) (2024) 1219.
[52] P. Petchimuthu, G.B. Sumanth, S. Kunjiappan, S. Kannan, S.R.K. Pandian, K. Sundar, Green extraction and optimization of bioactive compounds from Solanum torvum Swartz. Using ultrasound-aided solvent extraction method through RSM, ANFIS and machine learning algorithm, Sustain. Chem. Pharm. 36 (2023) 101323.
[53] H. Shen, Y. Zheng, R. Chen, X. Huang, G. Shi, Neuroprotective effects of quercetin 3-O-sophoroside from Hibiscus rosa-sinensis Linn. On scopolamine-induced amnesia in mice, J. Funct. Foods. 76 (2021) 104291.

[54] Y. Song, X. Wang, S. Qin, S. Zhou, J. Li, Y. Gao, Esculin ameliorates cognitive impairment in experimental diabetic nephropathy and induces anti-oxidative stress and anti-inflammatory effects via the MAPK pathway, Mol. Med. Rep. 17 (5) (2018) 7395–7402.
[55] A. Merlicco, Neuroprotective activity of guanosine in an in vitro model of Alzheimer's disease, (2009).
[56] A.V. Srivathsa, N.M. Sadashivappa, A.K. Hegde, S. Radha, A.R. Mahesh, D. N. Ammunje, D. Sen, P. Theivendren, S. Govindaraj, S. Kunjiappan, A review on artificial intelligence approaches and rational approaches in drug discovery, Curr. Pharm. Des. 29 (15) (2023) 1180–1192.
[57] A.K. Kalimuthu, T. Panneerselvam, P. Pavadai, S.R.K. Pandian, K. Sundar, S. Murugesan, D.N. Ammunje, S. Kumar, S. Arunachalam, S. Kunjiappan, Pharmacoinformatics-based investigation of bioactive compounds of Rasam (South Indian recipe) against human cancer, Sci. Rep. 11 (1) (2021) 21488.
[58] A. Sathiyaseelan, K. Saravanakumar, A.V.A. Mariadoss, K.M. Kim, M.-H. Wang, Antibacterial activity of ethyl acetate extract of endophytic fungus (Paraconiothyrium brasiliense) through targeting dihydropteroate synthase (DHPS), Process Biochem. 111 (2021) 27–35.
[59] S. Vellur, P. Pavadai, E. Babkiewicz, S. Ram Kumar Pandian, P. Maszczyk, S. Kunjiappan, An in silico molecular modelling-based prediction of potential Keap1 inhibitors from Hemidesmus indicus (L.) R. Br. against oxidative-stress-induced diseases, Molecules. 28 (11) (2023) 4541.
[60] M.L. Marcovecchio, Complications of acute and chronic hyperglycemia, US. Endocrinol. 13 (1) (2017) 17–21.
[61] S.P. Wolff, Z.Y. Jiang, J.V. Hunt, Protein glycation and oxidative stress in diabetes mellitus and ageing, Free Radic. Biol. Med. 10 (5) (1991) 339–352.
[62] O.I. Aruoma, V.S. Neergheen, T. Bahorun, L.-S. Jen, Free radicals, antioxidants and diabetes: embryopathy, retinopathy, neuropathy, nephropathy and cardiovascular complications, Neuroembryology. Aging 4 (3) (2007) 117–137.
[63] D.G.d. Freitas Pires, L.M.d. Araújo, P.G. Mesquita, F.d.A.R. Neves, M.d.F. Borin, Antioxidant activity of mycelia methanolic extracts of endophytic fungi BvFV and BvFIX isolated from leaves of Bauhinia variegata, Front. Fungal. Biol. 3 (2022) 1048734.
[64] A.M. Duarte, M.P. Guarino, S. Barroso, M.M. Gil, Phytopharmacological strategies in the management of type 2 diabetes mellitus, Foods. 9 (3) (2020) 271.
[65] Y.K. Kodagoda, C.V.L. Jayasinghe, R.M. Dharmadasa, In vitro antioxidant activity and antidiabetic potential of five spiral ginger (Costus speciosus (J. Koenig) Sm.) populations available in Sri Lanka, J. Agric. Food Res. 12 (2023) 100553.